A Laboratory Study of the Zonal Structure of Western Boundary Currents

STEFANO PIERINI
Dipartimento di Scienze per l'Ambiente, Università di Napoli Parthenope, Naples, Italy

VINCENZO MALVESTUTO
Istituto di Scienze dell'Atmosfera e del Clima, CNR, Rome, Italy

GIUSEPPE SIENA
CONISMA, Milazzo, Italy

THOMAS A. MCCLIMANS AND STIG M. LØVÅS
SINTEF, Trondheim, Norway

(Manuscript received 27 September 2006, in final form 24 August 2007)

ABSTRACT

The zonal structure of strongly nonlinear inertial western boundary currents (WBCs) is studied experimentally along a straight "meridional" coast in a 5-m-diameter rotating basin by analyzing the "zonal" profile of the meridional velocity field as a function of transport intensity and other dynamical parameters. The return flow that is generated by the surface wind stress curl in the oceanic interior is forced in the rotating basin by the motion of a piston, in the absence of any surface stress. The laboratory setup consists of two parallel rectangular channels separated by an island and linked by two curved connections: in the first channel, a piston is forced at a constant speed u_p ranging from 0.5 to 3 cm s^{-1} over a distance of 2.5 m, producing a virtually unsheared current at the entrance of the second channel. In the latter, a linear reduction of the water depth provides the topographic beta effect that is necessary for the development of the westward intensification. Nearly steady currents are obtained and measured photogrammetrically over a region of about 1 m^2. In all of the experiments performed, an appropriate horizontal Reynolds number (Re = ε/E, where ε and E are dimensionless numbers measuring the importance of nonlinearity and lateral friction, respectively) is Re $\gg 1$. The zonal profile of the meridional velocity is always found to have (away from the viscous boundary layer) a nearly exponential structure typical of inertial WBCs, whose width agrees well with the classical inertial boundary layer length scale δ_I. A control experiment (with u_p = 1 cm s^{-1}) is analyzed in detail: it has the same ε as the Gulf Stream (GS) but a much smaller E. This implies that the laboratory flow is expected to be geometrically similar to the GS outside the viscous boundary layer, but to differ within it. To assess the effect of such a departure from dynamic similarity, a mathematical model is used that numerically simulates a flow that is fully dynamically similar to the GS. The comparison between the profile thus obtained numerically and the one obtained experimentally shows that they are, indeed, virtually coincident outside the viscous boundary layer, except for a small offset that tends to vanish as Re $\to \infty$. Moreover, additional sensitivity experiments in which the piston speed, the rotation rate of the basin, the topographic beta effect, and the width of the main channel are varied provide further information on the zonal structure of WBCs.

1. Introduction

Western boundary currents (WBCs) are fundamental features of the large-scale wind-driven ocean circulation. In the subtropical (subpolar) gyres they are narrow and intense poleward (equatorward) currents [e.g., the Gulf Stream (GS) in the North Atlantic, the Kuroshio and Oyashio in the North Pacific, and the East Australian Current in the South Pacific, etc.] that play a fundamental role in the global climate, as they provide a substantial fraction of the oceanic meridional heat transport. Moreover, their peculiar geographical structure can have important implications on the climate of vast areas. For instance, the northern Gulf Stream branch of warm surface waters that flows north

Corresponding author address: Stefano Pierini, Dipartimento di Scienze per l'Ambiente, Università di Napoli "Parthenope," Centro Direzionale, Isola C4, 80143 Napoli, Italy.
E-mail: stefano.pierini@uniparthenope.it

DOI: 10.1175/2007JPO3706.1

of the British islands, the so-called North Atlantic Drift, contributes to make surface temperatures in northwestern Europe significantly higher than those typical of other regions at the same latitude. Complex mechanisms involving the wind-driven and thermohaline circulation and water mass transformation, and those related to the current global warming, might induce a weakening of such northward heat transport, with possible dramatic changes in the climate of northwestern Europe (e.g., Rahmstorf 1997, 1999). These examples show how important it is to improve our understanding of the functioning of WBCs. An enormous amount of work has been carried out on WBC dynamics and thermodynamics, both of a theoretical nature and through experimental and numerical simulations, since Stommel (1948) and Munk (1950) explained the basic linear dynamical mechanisms that generate westward intensification of the meridional currents deriving from the return flow of the Sverdrup (1947) transport produced in the oceanic interior by the wind [for theoretical accounts on basic aspects of WBCs see, e.g., Gill (1982) and Pedlosky (1987, 1996)].

In the last few decades numerical simulations have almost always complemented analytical treatments in the investigation and interpretation of basic mechanisms of physical oceanography; nonetheless, a small but significant amount of experimental simulations based on the use of rotating basins and the principle of dynamic similarity have been carried out as well (e.g., see Faller 1981 for a summary), and in this context WBCs have been analyzed in several cases. The main approach is based on the so-called sliced cylinder model (e.g., Pedlosky and Greenspan 1967; Greenspan 1969; Beardsley 1969; Beardsley and Robbins 1975; Pedlosky et al. 1997; Griffiths and Kiss 1999; Helfrich et al. 1999; Deese et al. 2002) in which a homogeneous fluid contained in a cylinder with a planar sloping bottom (that introduces an equivalent topographic beta effect) is driven by a rotating upper lid in order to bypass the technical and dynamical problems related to the forcing by a real wind in the laboratory. A generalization of this model that takes into account the effect of sloping sidewalls is known as the sliced cone model (Griffiths and Veronis 1997, 1998). See Kiss (2001) for an excellent and exhaustive analysis of the sliced cylinder and cone models.

These laboratory models are, in fact, conceived to simulate an idealized subtropical gyre, of which the WBC is only (an extremely significant) part of the flow: this requires a basinwide surface forcing, and the resulting zonal extension of the WBC is, consequently, of only a few centimeters width (also because of the relative smallness of the rotating tanks used, usually of about 1 m in diameter). Moreover, the WBCs thus obtained are in a linear or moderately nonlinear regime. On the other hand, it is well known that real WBCs in the world's oceans are strongly nonlinear (e.g., Pedlosky 1996). It appears, therefore, worthwhile to consider alternative experimental setups in large rotating basins that allow one to investigate aspects that have not been completely addressed in the laboratory models mentioned above, namely, (i) the behavior of WBCs in a parameter range in which nonlinear effects are as strong as in real oceans and (ii) a zonal extension of the WBC that is much larger than a few centimeters, so as to be able to resolve adequately the profile of the alongshore velocity.

The laboratory study presented in this paper meets these two requirements, as it deals with wide and strongly nonlinear WBCs. The basic idea [inspired by the companion laboratory study of topographic Rossby normal modes of Pierini et al. (2002)] is that, assuming the effect of the wind in the WBC region is negligible (e.g., Pedlosky 1987), then, if only the zonal structure of a WBC (and not also the whole gyre) is to be investigated, the return Sverdrup flow generated by the wind in the oceanic interior can be substituted by a remote mechanical production of a flow provided by the motion of a piston, in the absence of any surface stress. This was achieved in the 5-m-diameter rotating basin at the Foundation for Industrial and Technological Research at the Norwegian Institute of Technology (SINTEF), in Trondheim (Norway), by using two parallel rectangular channels separated by an island and linked by two curved connections. In the first channel, a piston was forced at a constant speed, producing a virtually unsheared current at the entrance of the second channel. In the latter, a downstream linear reduction of the water depth provided the topographic beta effect necessary for development of the westward intensification [this geometry shares some similarity with that adopted by Baines and Hughes (1996) in a 1-m-diameter rotating basin, but in their case a downchannel sloping surface lid was present and the flow was forced through a pump system]. Thanks to the large dimension of the present basin (and therefore of the channel along which the piston moves), and to the possibility of impressing relatively large velocities to the piston, large water transports are provided at the entrance of the sloping channel where strongly nonlinear WBCs are generated. Moreover, due to the large dimension of the tank, zonal extensions $O(1\text{ m})$ are achieved for the modeled WBCs. The fundamental question considered in the present paper is how the zonal structure of a WBC behaves for varying intensity and/or other parameters. This is answered through a set

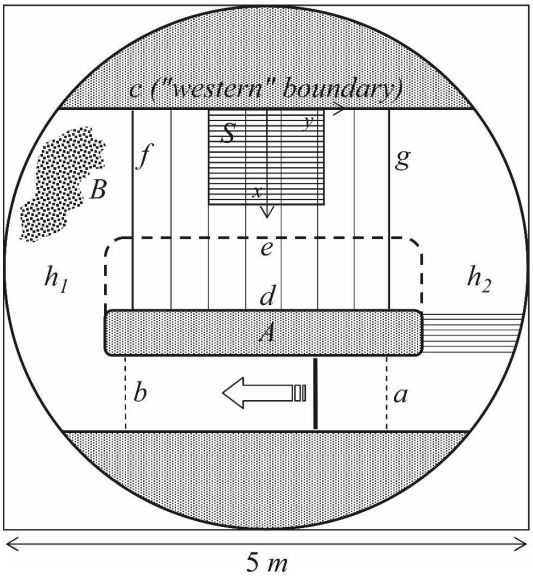

diameter of the tank:	5 m
distance (from *a* to *b*) covered by the paddle:	2.5 m
length of the paddle:	0.69 m
width of the paddle:	2 cm
width of the paddle channel:	0.7 m
length of the "island" *A*:	3.05 m
distance between *c* and *d*:	1.9 m
distance between *c* and *e*:	1.2 m
length of the bottom slope (from *f* to *g*):	2.4 m
dimension of the area *S* covered by the photogrammetry:	1.1 m x 0.90 m
maximum water depth (h_1):	40 cm
minimum water depth (h_2):	15/17/27.5 cm

FIG. 1. Experimental setup (the various dimensions are shown in the table): B denotes the region where the buoys are seeded before the piston starts moving.

of laboratory experiments designed in synergy with a numerical model based on the shallow-water equations. The experimental program is explained in section 2. In section 3, example results are discussed in terms of the theoretical foundations for WBCs and are compared with numerical simulations. The remainder of the experiments are presented and discussed in section 4. Conclusions and future perspectives are discussed in the concluding section 5.

2. Experimental setup and measuring technique

The experimental approach adopted for modeling WBCs is based on the assumption that the effect of wind in the WBC region is negligible. Thus, if only the zonal structure of a westward-intensified poleward current is to be investigated, then the return flow generated by the surface wind stress curl in the oceanic interior (which turns poleward when entering the western boundary region, thus feeding the WBC) can be substituted by a remote mechanical production of a flow provided by the motion of a piston, in the absence of any surface stress. As for the minor role played locally by the wind in the narrow WBC region of a subtropical gyre, apart from any rigorous scaling argument [which can be found in Pedlosky (1987)], one can easily understand that such an effect is small because the water column spends a short time in the boundary region as it moves poleward with a strong meridional velocity; in addition, that area is of very limited extent. As a consequence, the rate of input of vorticity from the wind is accordingly small if compared with other effects, such as dissipation and the increase of planetary vorticity as the water column moves poleward.

The experimental setup was inspired by the one used by Pierini et al. (2002) to model topographic Rossby normal modes in the "Coriolis" rotating tank at the Laboratoire des Ecoulements Geophysiques et Industriels (LEGI) of the Centre National de la Recherche Scientifique (CNRS) in Grenoble (France), but for the present experiments substantial modifications have been necessary. The setup is shown in the plan view of Fig. 1 (relevant dimensions are given in the box on the right): it consists of two parallel rectangular channels separated by an island (A) and linked by two curved connections. In the lower narrow channel, a piston was forced leftward at a constant speed over a distance of 2.5 m (between lines a and b), producing a virtually unsheared current at the entrance of the main upper channel. In the latter, a northward (to the right in this view) linear reduction of the water depth (between lines f and g) provides the topographic beta effect necessary for the formation of the westward intensification along line c as a consequence of the conservation of potential vorticity of water columns entering the bottom slope past line f (notice that, because of the depth variation and of the small parabolic deformation of the free surface due to rotation, the topographic beta effect is not exactly constant, yielding a weak dependence on *x* and *y* over the slope; nonetheless a constant mean value is considered in the theoretical arguments presented in section 3, focused on the small portion S of

the slope—see below). The horizontal lines to the right of the island A are the isobaths where the bottom descends from depth h_2 to the lower level of depth h_1 where the piston drives the circulation.

Since nearly steady WBCs are desired, one of the problems that had to be solved in planning the experimental setup was to avoid, as much as possible, the excitation of energetic topographic Rossby normal modes (Pierini et al. 2002) on time scales comparable to or longer than the duration of the experiment (basically equal to the time over which the piston is in motion). Those waves would not only constitute a noise superimposed on the dynamics under investigation but might even affect the structure of the boundary current through nonlinear interactions. The sizes of the channel and of the bottom slope were determined also in view of this requirement, and the results have confirmed that some Rossby wave activity contaminates the WBC only in the few experiments that have a very limited duration because of the large speed of the piston, as will be seen below.

The speed of the piston u_p determines the total transport, whose value is expected to be of fundamental importance in the generation of highly nonlinear WBCs (section 3b). Such speed had lower and upper limits; for example, u_p could not be smaller than ~ 0.5 cm s^{-1} because below that threshold the mechanical apparatus that generated the piston motion could not have a perfectly constant speed. On the other hand, for $u_p > 3$ cm s^{-1}, the motion lasted for less than ~ 80 s, which is insufficient to reach an almost steady state (moreover, larger speeds induced a significant gravity wave signal that distorted the currents under investigation). Therefore, the following four values of the piston speed were chosen: $u_p = 0.52$, 1, 2, and 3 cm s^{-1}.

After the homogeneous water came into solid body rotation and before starting the piston, several hundred small buoys were seeded over the entrance of the main channel (in the region B sketched in Fig. 1). These were then advected by the currents to the region of interest. The velocities of the buoys were measured photogrammetrically over the region S of about 1 m^2, which is the field of view of the photogrammetry system, placed where the WBCs are almost purely alongshore. Three cameras were mounted on a frame about 2 m above the water surface. The position and orientation of the cameras was obtained through a calibration procedure described in Nilsen and Hådem (1994). Through photogrammetry the cameras allowed us to compute the 3D position of dark particles above an illuminated background. In the present application, however, only the two horizontal coordinates are of interest since the surface is essentially constant in time. The system does, however, reveal the parabolic surface of the rotating fluid in accordance with the rotation rate.

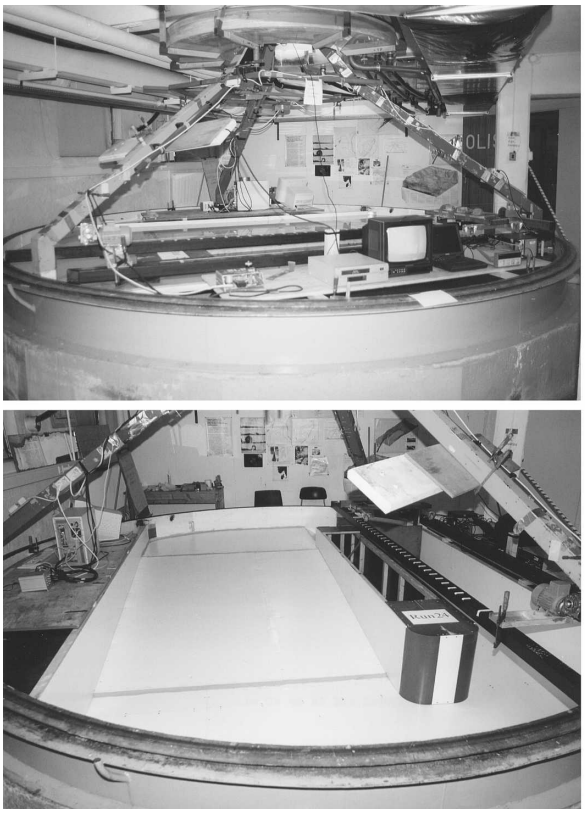

FIG. 2. Photos showing (a) an overall view of the experimental apparatus and (b) the bottom topography and piston system adopted in the experiments.

Using particle tracking techniques, the particle positions from each image are connected in time traces, allowing the computation of velocity vectors. The system was developed at SINTEF (Nilsen and Hådem 1994) and further refined during the European Union (EU) Fifth Framework Program as part of the development and implementation of novel imaging velocimetry techniques suited to large-scale hydraulic facilities (HYDRIV; Contract HPRI-CT-1999–50019). A more detailed description of the system used and an application is given by Løvås (2003) and Løvås et al. (2001). In addition to the photogrammetry, there was a wide-angle video camera (backup), providing a time lapse record to monitor the experiments and confirm that the piston motion and general circulation behaved well. In Fig. 2 two photographs of the facility with the experimental topography in place are shown: the steering and measuring equipment can be seen on the instrument tables. In Fig. 2a the variable-speed control of the piston and the monitoring equipment are seen, and the time-lapse recorder is shown. The equipment to the left

TABLE 1. List of all the experiments; those in parentheses have already been reported above.

Expt	$d(c, A)$ (cm)	$h_1 - h_2$ (cm)	T_{rot} (s)	u_p (cm s^{-1})	Comments
A	120	25	30	0.52	Varying paddle speed (small differences in the setup)
B	190	23	30	1	
C	190	23	30	2	
D	120	25	30	3	
(B)	190	23	30	1	Varying rotation rate, small island, $u = 1$ cm s^{-1}
E	190	23	45	1	
F	190	23	60	1	
(C)	190	23	30	2	Varying rotation rate, small island, $u = 2$ cm s^{-1}
G	190	23	45	2	
H	190	23	60	2	
I	190	12.5	30	1	Varying rotation rate, small island, small slope height
J	190	12.5	45	1	
K	190	12.5	60	1	
L	120	25	30	1	Varying rotation rate, large island, $u = 1$ cm s^{-1}
M	120	25	45	1	
N	120	25	60	1	
O	120	25	30	2	Varying rotation rate, large island, $u = 2$ cm s^{-1}
P	120	25	45	2	
Q	120	25	60	2	
R	120	12.5	30	1	Varying rotation rate, large island, small slope height
S	120	12.5	45	1	
T	120	12.5	60	1	
U	120	0	30	1	No beta effect
V	120	25	∞	1	No rotation

in Fig. 2b shows the computer that processes the particle tracking velocimetry (PTV) data.

3. A set of basic experiments

Several experiments were carried out in order to analyze the effect of varying the transport, the topographic beta effect, and the width of the main channel on the zonal structure of the WBC. The first variation was obtained by changing the piston speed; the second variation was obtained by varying the rotation rate of the tank and/or the bottom slope by modifying the minimum water depth h_2; and, finally, the third variation was achieved by changing the width of the island A from line d to line e (see Fig. 1). Although all of the experiments performed are significant, those that focus on the response of the WBC to different transport values are most relevant as their analysis can contribute to the understanding of low-frequency variability of oceanic WBCs (WBCs with different total transports can be seen as different states of the same system resulting from slow variations of the large-scale wind forcing). For this reason we begin by presenting, in section 3a, four experiments (A, B, C, and D; see Table 1) that differ only by the speed of the piston. In section 3b theoretical considerations are presented to put the results in the correct dynamical framework, and in section 3c the experiments are compared with numerical simulations, and theoretical conclusions are drawn in connection to the scaling to real WBCs. The remaining sensitivity experiments will be presented in section 4.

a. Four experiments differing in flow intensity

Here we present and discuss experiments A, B, C, and D (see Table 1) that differ only by the speed of the piston ($u_p = 0.52$ cm s^{-1} for experiment A, $u_p = 1$ cm s^{-1} for experiment B, $u_p = 2$ cm s^{-1} for experiment C, and $u_p = 3$ cm s^{-1} for experiment D), all other parameters remaining unchanged apart from a variation in the width of the main channel (120 cm for experiments A and D, and 190 cm for experiments B and C; in section 4 it will be shown that decreasing the width of the main channel has, generally, only a minor effect on the WBC, but see the discussion of Fig. 5a in section 3 for an effect induced by width variation) and a minor

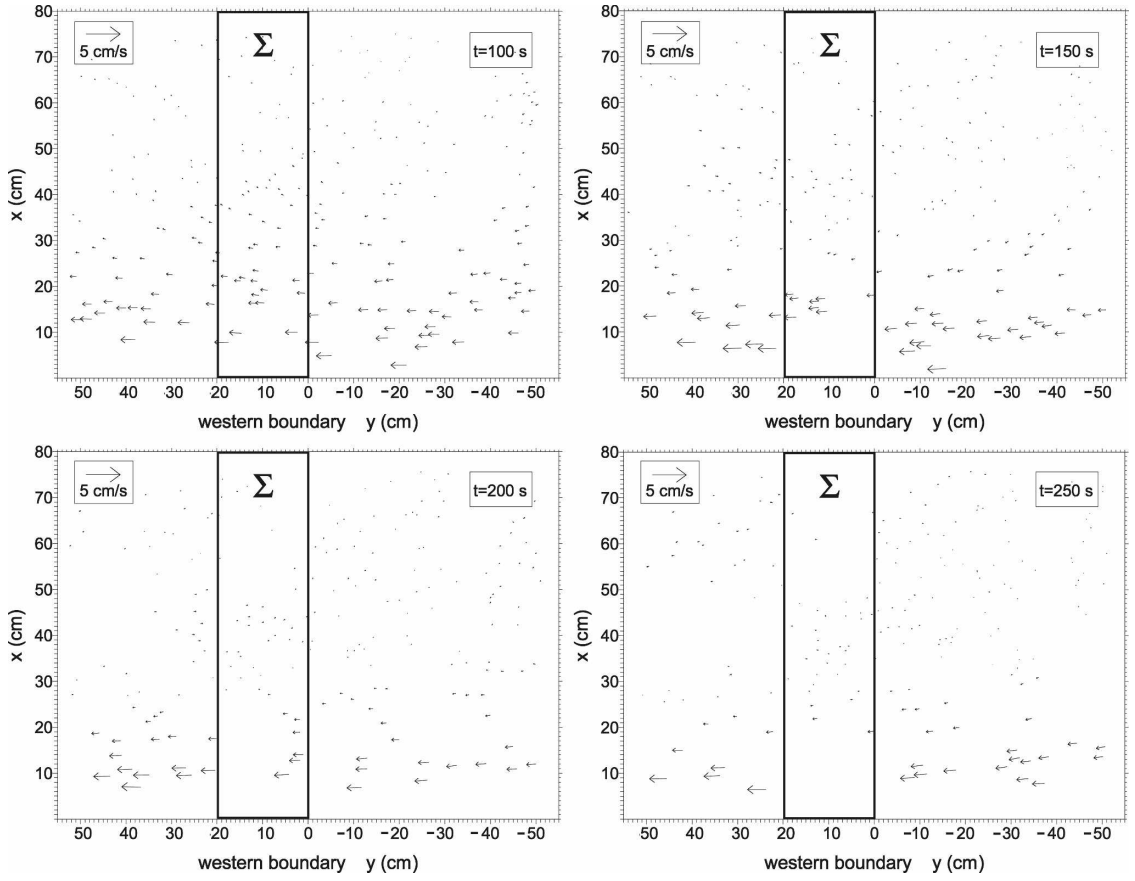

FIG. 3. Velocities of the buoys measured by the photogrammetry in sector S (Fig. 1) at four different times (t = 100, 150, 200, 250 s) for expt A. The rectangle Σ denotes the area within which velocities are averaged.

variation in the height of the bottom slope (25 cm for experiments A and D, and 23 cm for experiments B and C). Experiments with exactly the same parameters (except the piston speed) in all four experiments were, in fact, performed but the quality of the measurements was not uniformly good, so we must rely on these "virtually homogeneous" experiments for which all of the data are excellent.

Figure 3 shows examples of instantaneous velocities (for experiment A) obtained by the measuring technique described in section 2 (the position of each arrow gives the location of the corresponding particle). To obtain a significant velocity profile, an averaging procedure over both space and time had to be applied. The spatial average was performed in different portions of sector Σ, which is 20 cm wide along y and is centered at y = 10 cm (this position is a little farther downstream with respect to the center of the main channel at y = 0 because there the flow is virtually alongshore, as evidenced by the numerical simulation reported later in Fig. 8). A first analysis of the experimental results concerns the time evolution of the gross features of the flow, as this allows us to monitor the adjustment process. In Fig. 4 the time series of the alongshore component v, obtained by averaging spatially within Σ over four sectors of 20-cm width along x (line 1, etc., refer to x = 0–20 cm, etc.) and temporally over 10-s intervals are shown. The westward intensification is evident and so is the strongly nonlinear character of the dynamics under investigation. At t = 0 the piston starts moving, reaching maximum speed almost immediately. Within about 3 s, the water is in motion in sector S; this is the time needed for long surface gravity waves to cover the distance between lines a and f. The spinup leading to the westward intensification of the current is a much slower process involving the propagation of (topographic) barotropic Rossby waves (Pedlosky 1965). The initial excitation of Rossby waves, evident in the oscillations that last until t ~120–140 s, is followed by a much less variable, almost steady, state in experiments A and B, lasting until spindown begins following the arrest of the piston (indicated by the vertical line). In experiments C and D the spinup is not complete, especially in the second experiment, yet the data, though

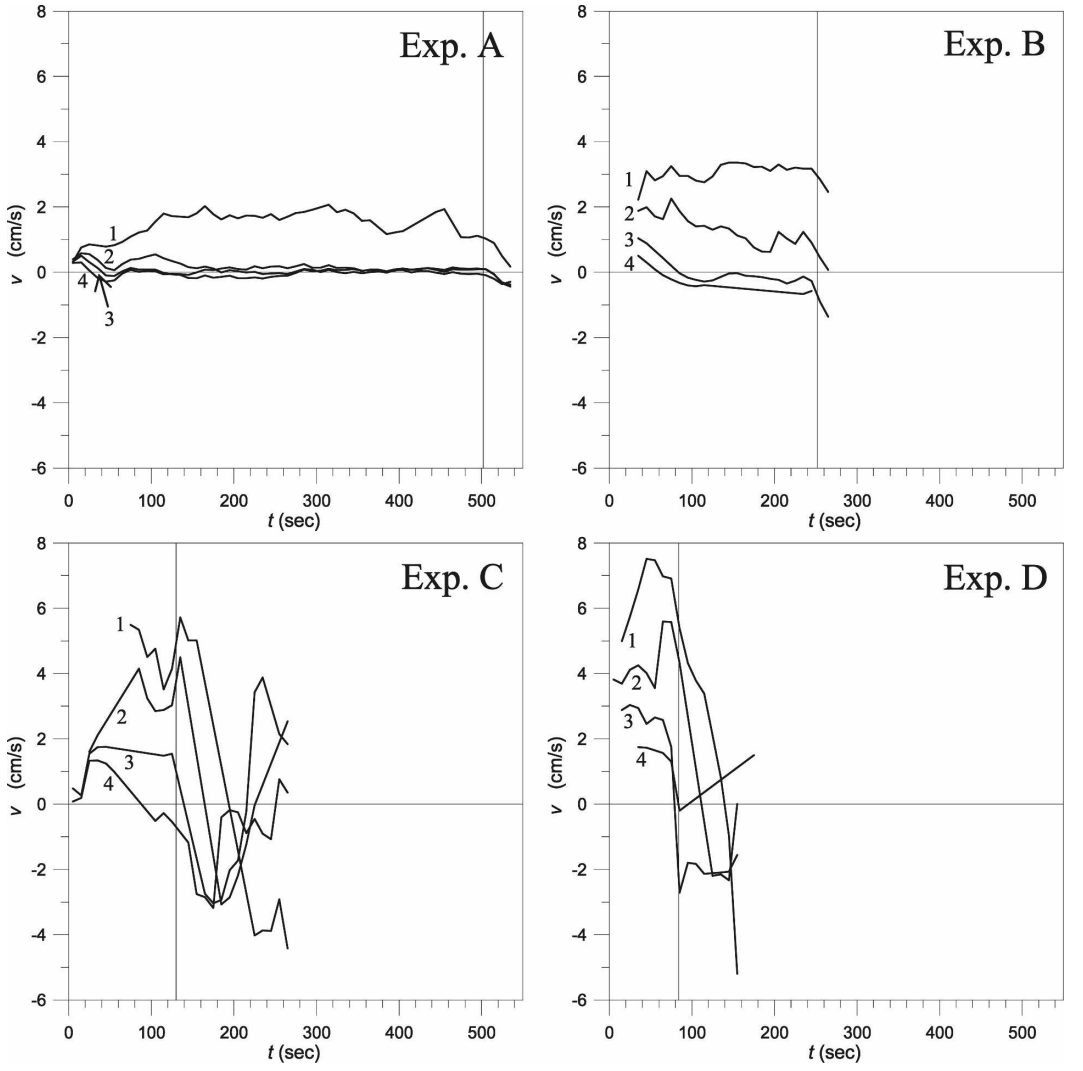

FIG. 4. Time series of the alongshore component v of the velocity measured by photogrammetry in experiments A, B, C, and D and averaged over sectors delimited in y by 0–20 cm and in x by 0–20 cm (line 1), 20–40 cm (line 2), 40–60 cm (line 3), and 60–80 cm (line 4). The sum of these four sectors gives the sector denoted as Σ in Fig. 3. The vertical line indicates the time when the piston stops.

contaminated by Rossby waves, are valuable in these cases as well, as discussed in section 3c.

In Fig. 5 each bar represents a velocity value v relative to $y = 10$ cm obtained by averaging spatially within the 0–20-cm interval in the y direction and over a sector 2 cm wide in the x direction and temporally over the following intervals (based on the results of Fig. 4): 100–460 s for experiment A, 80–240 s for experiment B, 60–130 s for experiment C, and 40–80 s for experiment D. A first comparison of the four cases shows that the flows considered belong to a strongly nonlinear regime (and, indeed, the profile west of the counterflow appears to have an exponential form typical of inertial WBCs). For instance, the total "meridional" transport Q of experiment A is obviously half that of experiment B, but the "zonal" profile of the meridional velocity of experiment A is far from being equal to that of experiment B scaled by a factor of 0.5 (as would be the case if we were in a linear regime), and the same can be said if experiment B were compared with experiment C. Figure 6a shows, rather, that the maximum velocity $v_{\max}$ measured in each experiment is nearly proportional to the square root of u_p (dashed line; the solid line indicates linear dependence); the remaining transport is gained through a larger zonal extension of the current system determined by the position of the stagnation line x_s (representing a good zonal length scale of the WBC) beyond which there is a counterflow (Fig. 6b). In fact, x_s shifts more and more offshore as u_p increases (the counterflow to the right of the stagnation line must

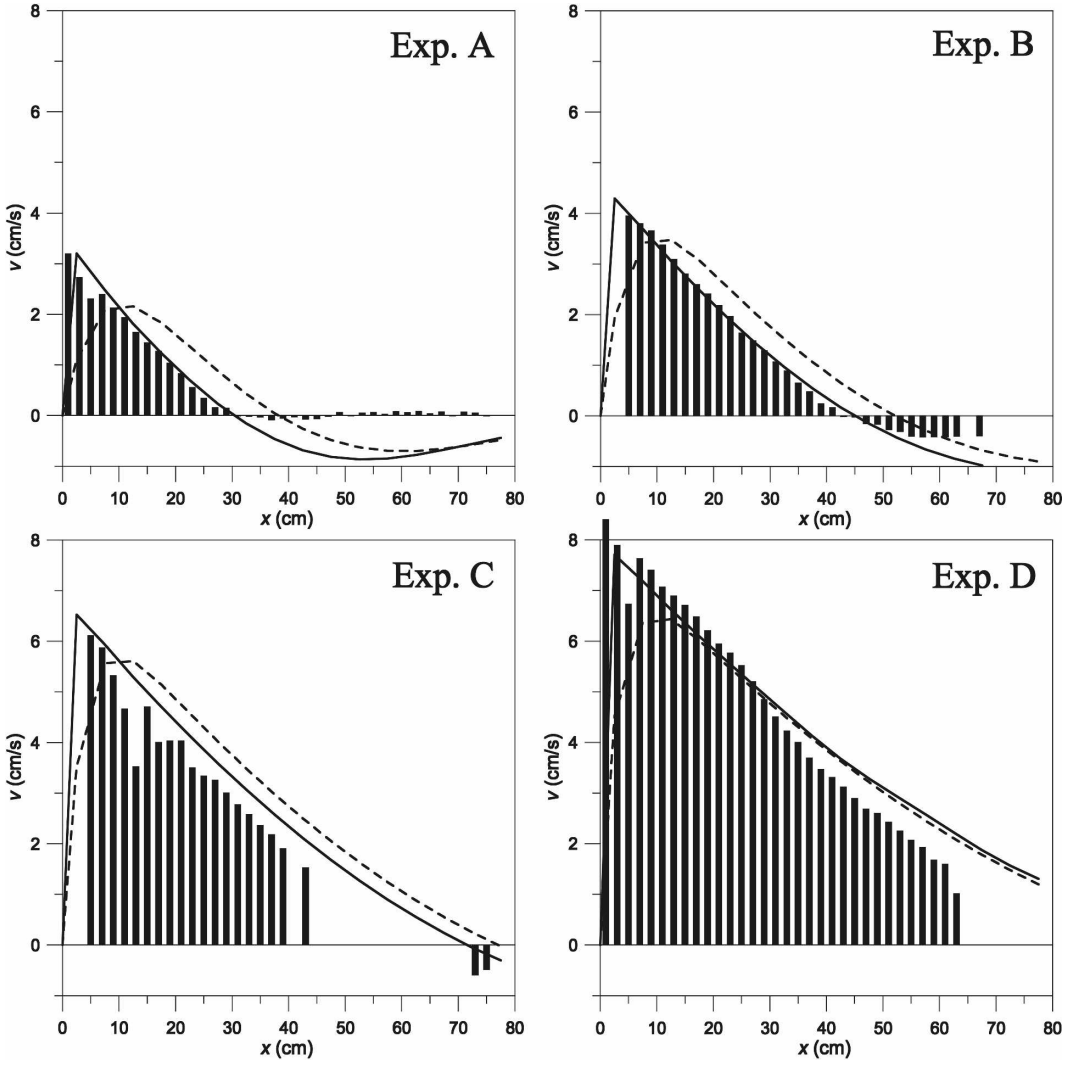

FIG. 5. Zonal profiles of the alongshore component v of the velocity obtained by photogrammetry (bars) and numerical simulations (lines) for expts A, B, C, and D. Each bar represents a velocity centered at $y = 10$ cm and averaged spatially over a sector 2 cm wide in the x direction and within the interval 0–20 cm in the y direction; the velocity is averaged over the intervals 100–460 s for expt A, 80–240 s for expt B, 60–130 s for expt C, and 40–80 s for expt D. The lines show v at $y = 10$ cm obtained numerically (see section 3c) for $A = 10^{-6}$ m^2 s^{-1} (solid lines) and $A = 10^{-4}$ m^2 s^{-1} (dashed lines) at $t = 120$ s (expt A), $t = 90$ s (expt B), $t = 60$ s (expt C), and $t = 30$ s (expt D). The dashed lines refer to case DSGS that is dynamically similar to the Gulf Stream.

also be considered in an exact evaluation of the total transport). It should be noticed, however, that in experiment D no counterflow is present (moreover, no data are available for $x > 65$ cm). Thus, in this case an effective x_s (again, interpreted merely as a zonal length scale) is computed by fitting the profile exponentially and choosing x_s as the distance from the boundary where the maximum velocity value is decreased by an arbitrary factor 0.9 ($x_s \approx 80$ cm).

The increase of x_s is in basic agreement with the dependence of the zonal length scale of inertial WBCs on flow intensity. This will be considered in detail in the next subsection, but, assuming for the moment that (as we have already noticed qualitatively) we are dealing with highly nonlinear flows, we can anticipate that the zonal extent of the boundary current is expected to behave like the classical width of inertial WBCs, that is, $\delta_I \propto \sqrt{u_p}$ [see Eq. (7) below], and it also seems reasonable to assume $x_s \propto \delta_I$. This can be verified by noting the good agreement between the actual value of x_s given by the bars and the fit proportional to the square root of u_p given by the dashed line in Fig. 6b. Finally, Fig. 6c shows x_s as a function of the maximum velocity: their nearly linear relation reflects the fact that both x_s

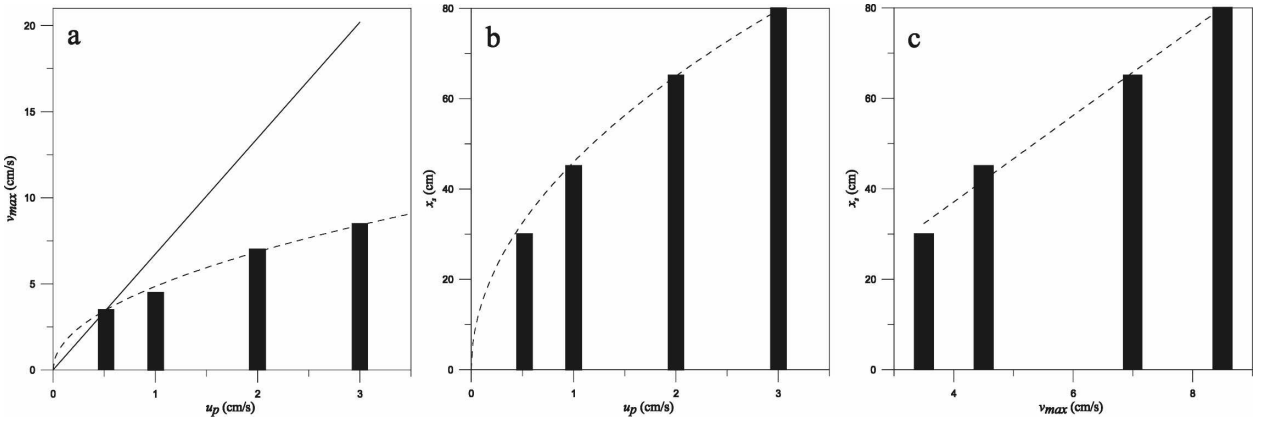

FIG. 6. (a) Maximum velocity $v_{\max}$ measured in each experiment vs u_p (bars), fit proportionally to the square root of u_p (dashed line) and the linear trend to be expected in the linear regime (solid line); (b) zonal location x_s of the stagnation point vs u_p (bars), fit proportionally to the square root of u_p (dashed line); and (c) x_s vs $v_{\max}$ (bars) and the linear fit (dashed line).

and $v_{\max}$ depend on the square root of u_p so that the total volume transport Q, approximately proportional to the product $x_s v_{\max}$, is in turn proportional to u_p, as it should be; moreover, the slope of the nearly triangular velocity profile west of x_s remains virtually constant in this parameter range (this is also evident from Fig. 5).

In section 3b, experiment B (chosen as a reference case) will be analyzed theoretically in order to relate it to a real WBC. The other three cases considered here can be seen as representative of states associated with the low-frequency variability of the phenomenon, and will be considered in section 3c.

b. Scaling and theoretical considerations

Let us start from the most general evolution equation for the potential vorticity of a layer of homogeneous and incompressible fluid over a flat bottom in the quasi-geostrophic approximation (e.g., Pedlosky 1996),

$$\frac{\partial}{\partial t}\left(\nabla^2\psi - \frac{\psi}{R^2}\right) + J(\psi, \nabla^2\psi) + \beta\psi_x = A_H\nabla^4\psi - r\nabla^2\psi + \frac{\mathrm{curl}_z\boldsymbol{\tau}}{\rho D}, \quad (1)$$

which can be used as a valuable diagnostic tool to study WBCs [its applicability in our case is ensured by the small value of the Rossby number $\varepsilon_R = U/(fl)$; see below for the definition of U, f, and l, e.g., $\varepsilon_R \approx 0.05$ for experiment B]. In (1) x is the zonal and y the meridional direction, the streamfunction ψ is related to the horizontal velocity through the relation $\mathbf{u} = (-\psi_y, \psi_x)$, β represents the variation of the Coriolis parameter with latitude (or an equivalent topographic beta effect, see below); $R = \sqrt{gD}/f_0$ is the external Rossby deformation radius [where g is the acceleration of gravity, D the water depth, and $f_0 = 2\Omega_{\mathrm{eff}}$ the Coriolis parameter [for f_0 the effective angular frequency is $\Omega_{\mathrm{eff}} = \Omega_{\mathrm{earth}}\sin\varphi$ in the real geophysical case, where φ is the latitude, while $\Omega_{\mathrm{eff}} = \Omega_{\mathrm{rot}} = 2\pi/T_{\mathrm{rot}}$ in the rotating tank experiments, where T_{rot} is the period of rotation of the tank]; A_H is the lateral eddy viscosity coefficient; $r = \sqrt{2A_v f_0}/2D$ (where A_v is the vertical eddy viscosity) is equal to the inverse of the spindown time due to bottom friction, ρ is the fluid density, and $\boldsymbol{\tau}$ is the surface wind stress. In our case, several terms can be neglected in (1). The experimental setup was conceived to model *steady* WBCs and, as seen in section 3a, the results have, indeed, provided for time intervals of significant duration (depending on the experiment) a virtually time-independent flow; therefore, the first two terms in the lhs of (1) can be neglected (note that the term in the potential vorticity representing the horizontal divergence of the currents does not appear in the nonlinear terms owing to an obvious property of the Jacobian operator, so the assumption of stationary flow removes any explicit dependence on both g and f_0). Moreover, as already discussed in sections 1 and 2, the wind gives a negligible contribution to the vorticity balance in the western boundary current region, so the last term in the rhs of (1) can be neglected. These approximations remove any explicit dependence on D (but the dependence on f_0 and D will appear again in the topographic beta effect β^*). The dynamics under investigation is therefore appropriately described by the steady and homogeneous version of (1), which, in view of the following scaling arguments, is advantageously written in terms of the velocity components:

$$u\nabla^2 v - v\nabla^2 u + \beta v \cong (A_H\nabla^2 - r)(v_x - u_y). \quad (2)$$

Let us now introduce the following scaling in which primed variables are dimensionless:

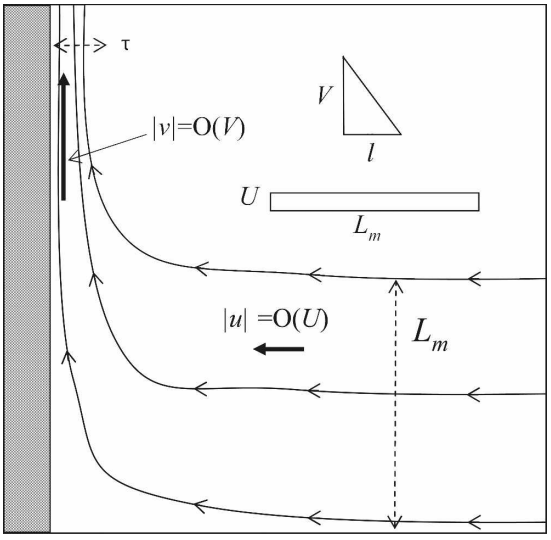

FIG. 7. Schematic representation of the return flow as it approaches the western boundary and the resulting WBC. The meaning of each parameter is discussed in section 3b.

$$x = lx'; \quad y = Ly'; \quad u = Uu'; \quad v = Vv'. \tag{3}$$

The values of these scaling parameters can vary notably according to whether the oceanic interior or the western boundary region is considered. In our case we are interested in the latter, for which $l \ll L$ and $V \gg U$, where l is the width of the WBC and L is the much larger meridional extension of the subtropical gyre. Moreover, while V is the order of magnitude of the strong meridional velocity of the WBC, U is a measure of the weak westward flow originating from the Sverdrup transport in the oceanic interior while veering poleward at the entrance to the boundary region (Fig. 7). The parameters U and V can be related by invoking mass conservation and a few other reasonable assumptions. Let us assume that in the low-latitude region (where the interior flow moves westward toward the western boundary) the current is constant in y and is limited within a meridional width L_m (Fig. 7), which we can assume to be roughly equal to $L_m \cong L/2$; the corresponding volume transport is therefore $Q = UL_m$. The same transport is found within the narrow boundary region, but now the assumption of uniform flow is not acceptable: We rather assume (also in view of Fig. 5) that the current profile is roughly represented by a triangle (this scaling argument is obviously not in contrast with the exponential character of the profile typical of inertial WBCs) so that the volume transport is $Vl/2$. Thus,

$$\frac{V}{U} = \frac{L}{l}. \tag{4}$$

By substituting (3) in (2), and considering that, thanks to the inequality $l \ll L$, one has $\nabla^2 \cong l^{-2}\partial^2/\partial x'^2$, Eq. (2) in dimensionless form is

$$\varepsilon(u'v'_{x'x'} - v'u'_{x'x'}) + v' \cong Ev'_{x'x'x'} - Bv'_{x'}. \tag{5}$$

The dimensionless parameters ε, E, and B measuring the importance of nonlinearities and lateral and bottom friction are given by

$$\varepsilon = \frac{U}{\beta l^2} = \left(\frac{\delta_I}{l}\right)^2; \quad E = \frac{A_H}{\beta l^3} = \left(\frac{\delta_M}{l}\right)^3; \quad B = \frac{r}{\beta l} = \frac{\delta_S}{l}, \tag{6}$$

where the length scales δ_I, δ_M, δ_S, and δ_E, defined as

$$\delta_I = \left(\frac{U}{\beta}\right)^{1/2}; \quad \delta_M = \left(\frac{A_H}{\beta}\right)^{1/3};$$
$$\delta_S = \frac{\delta_E f_0}{2D\beta}; \quad \delta_E = \left(\frac{2A_v}{f_0}\right)^{1/2}, \tag{7}$$

represent the boundary layer scales for a purely inertial (δ_I), purely viscous (δ_M) Munk (1950), and purely viscous (δ_S) Stommel (1948) flow, while δ_E is the thickness of the bottom Ekman layer (e.g., Pedlosky 1987, 1996; Hendershott 1987).

To relate the experimental results discussed in the preceding subsection to a full-scale WBC, we now evaluate the various parameters for both the oceanic flow, such as the Gulf Stream (taken as the prototype of this kind of dynamics, and denoted hereafter as GS), and the rotating tank (RT) experiment B, taken as a reference example; all parameters (both the basic and the derived ones) are summarized in Table 2. A typical width of the GS is $l \approx 100$ km, while in RT the width suggested by Fig. 5 is $l \approx 0.5$ m. A reasonable value $L_m \approx 1000$ km for the meridional extension of the westward flow in the GS can be assumed, while in the RT such a length scale is given by the width of the channel along which the piston moves: $L_m = 0.7$ m. The westward current parameter U for the GS can be evaluated by imposing in (4) a typical value $V = 1$ m s^{-1} for the maximum WBC speed, thus obtaining $U = 5$ cm s^{-1}, which is of the same order of magnitude of the parameter values used by Pedlosky (1987, 1996) and Hendershott (1987). For the RT, U is given by the piston speed, which for experiment B is $U = 1$ cm s^{-1} (this implies $V = 2.8$ cm s^{-1}, in good agreement with the observed speed). The lateral eddy viscosity coefficient in a real western boundary region is largely indeterminate, but we can assume, as a rough estimate, a typical and generally accepted value $A_H = 100$ m^2 s^{-1}. In the RT the kinematic viscosity coefficient for water applies: $A_H = 10^{-6}$ m^2 s^{-1} (the same value applies also to A_v for the

TABLE 2. Parameter values discussed in sections 3b, c.

Parameters	GS	RT expt B	DSGS
		Basic parameters	
l	100 km	0.5 m	0.5 m
L_m	1000 km	0.7 m	0.7 m
V	1 m s^{-1}	2.8 cm s^{-1}	2.8 cm s^{-1}
U	5 cm s^{-1}	1 cm s^{-1}	1 cm s^{-1}
A_H	100 m^2 s^{-1}	10^{-6} m^2 s^{-1}	10^{-4} m^2 s^{-1}
β	2×10^{-11} rad m^{-1} s^{-1}	0.14 rad m^{-1} s^{-1}	0.14 rad m^{-1} s^{-1}
		Derived length scales	
δ_I	50 km	27.00 cm	27.00 cm
δ_M	17 km	1.90 cm	8.90 cm
δ_S	—	1.10 cm	—
δ_E	—	0.22 cm	—
		Derived dimensionless parameters	
ε	2.5×10^{-1}	2.8×10^{-1}	2.8×10^{-1}
E	5.0×10^{-3}	5.7×10^{-5}	5.7×10^{-3}
Re	50	5000	49
B	—	2.3×10^{-2}	—

RT). The parameter β in the midlatitude ocean ($\varphi = 30°$) is $\beta = 2 \times 10^{-11}$ rad m^{-1} s^{-1}. In the RT the equivalent topographic beta effect is given by (Pedlosky 1987)

$$\beta^* = \frac{f}{H}\frac{d\gamma(y)}{dy}, \tag{8}$$

where H is an average depth, which in our case is $H = (h_1 + h_2)/2$ (see Fig. 1), and $\gamma(y)$ is the bottom topography. For experiment B one thus gets $\beta^* = 0.14$ rad m^{-1} s^{-1}.

The values obtained for the length scales in (7) and of the dimensionless parameters in (6) (Table 2) show that the RT experiment represents a nonlinear inertial case because $\delta_I \gg \delta_M, \delta_S$, confirming the heuristic discussion of section 3a. The inertial width $\delta_I = 27$ cm is of the same order as the observed WBC width, while the Stommel (1948) and Munk (1950) length scales of linear theories are only $\delta_S \approx 1$ cm and $\delta_M \approx 2$ cm; as a consequence, the nonlinear terms in (5), whose weight is $\varepsilon = 0.28 \gg E, B$, are predominant and balance the planetary vorticity gradient term. An analogous situation holds for the GS, with a value of ε very close to that of the laboratory experiment: $\varepsilon = 0.25 \gg E, B$. Thus, our experiment B (this scaling argument basically applies to all the other experiments as well) is a correct laboratory reference of full-scale WBCs.

However, this does not apply to a viscous layer near the wall where the two flows are not dynamically similar because the dimensionless parameters that express dissipation are different in the GS and the RT. Leaving aside bottom friction, which does not have a direct counterpart in real WBCs since the latter are greatly reduced near the bottom by baroclinic compensation (moreover, the numerical simulations presented in subsection 3c will show that its effect is virtually negligible everywhere in the RT), we can focus on the lateral viscosity. Its relative importance compared with inertial effects is given by a horizontal Reynolds number:

$$\mathrm{Re} = \frac{\varepsilon}{E} = \frac{Ul}{A} = \frac{\delta_I^2}{\delta_M^3}\, l. \tag{9}$$

In both RT and GS, Re $\gg$ 1, but two very different values apply—Re = 5000 and 50, respectively—and there was no way to match these two values because there were several technical problems in using a liquid with a molecular viscosity a hundred times that of water (considering the possible transition to turbulence with Re = 5000 in the laboratory, it is difficult to guarantee that the flow is truly laminar and that A_H is, indeed, the molecular value for the RT, but the numerical validation presented in section 3c ensures that any possible turbulent departure from the molecular viscosity has no appreciable relevance for the studied cases).

In summary, since both RT and GS cases fall under the nonlinear inertial regime with virtually the same ε, the two profiles away from the western boundary are expected to be geometrically similar but, near the boundary where viscosity acts to dissipate vorticity, they will not be similar because they have very different values of E (and so of Re). This hypothesis will be validated with the aid of a mathematical model in section 3c, where a fully dynamically similar GS case will be simulated numerically.

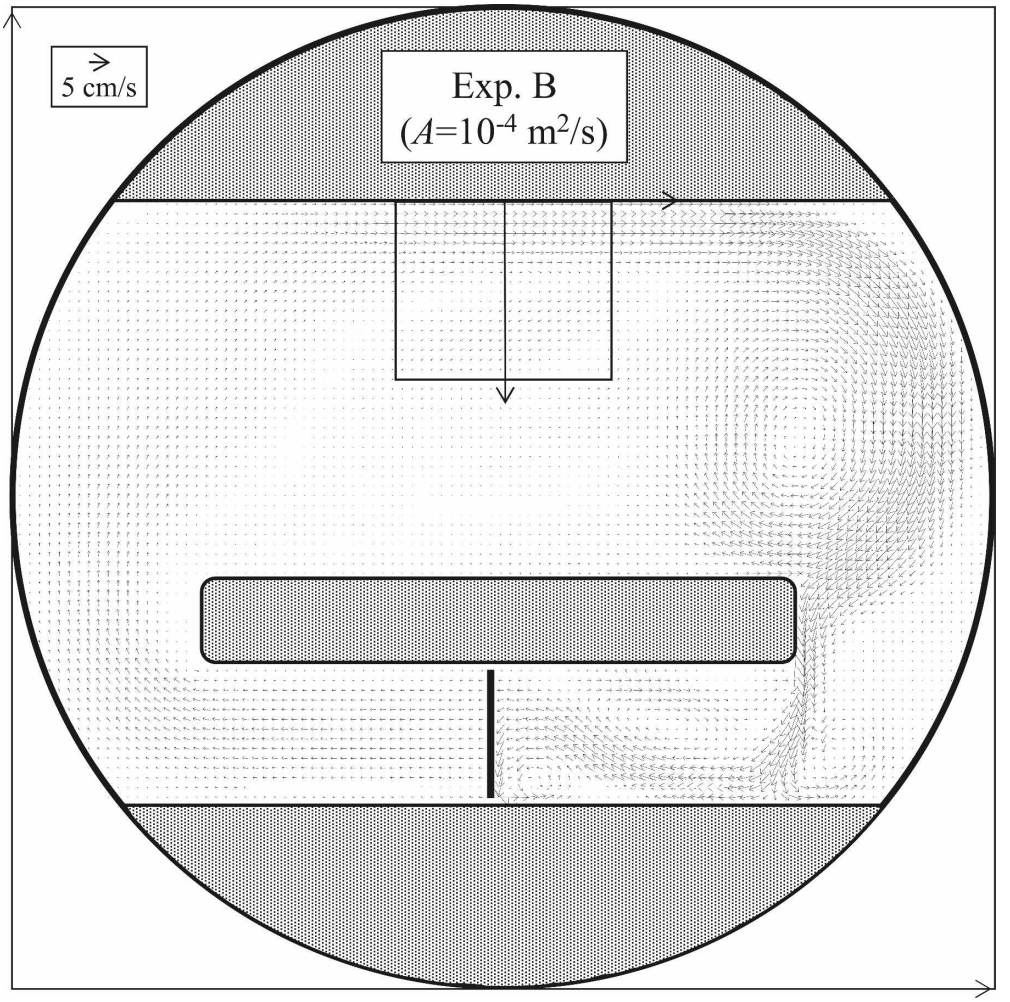

FIG. 8. Velocity field simulated numerically for expt B with $A = 10^{-4}$ m^2 s^{-1} at $t = 150$ s.

c. Numerical simulations and discussion

To assess the effect of departures from dynamic similarity in the RT and GS due to differences in Re, a mathematical model is used. The barotropic shallow-water equations for a homogeneous incompressible fluid [more general than Eq. (1)],

$$\mathbf{u}_t + (\mathbf{u}\cdot\boldsymbol{\nabla})\mathbf{u} + f\mathbf{k}\times\mathbf{u} = -g\nabla\eta + A_H\nabla^2\mathbf{u}$$
$$\eta_t + \boldsymbol{\nabla}\cdot(H\mathbf{u}) = 0, \qquad (10)$$

where η is the surface displacement and $\mathbf{k} = (0, 0, 1)$, are solved numerically through a finite difference scheme (e.g., Pierini 1996) in a domain that matches closely the experimental setup, as done in a similar context for another rotating tank experiment (Pierini et al. 2002). The piston motion is simulated by imposing a velocity normal to the piston profile with the same time dependence as the real one. The position of the "numerical" piston is held fixed, unlike the real one, but this does not have any significant effect on the induced flow away from the lower channel. The spatial grid steps are $\Delta x = \Delta y = 5$ cm and the time step is $\Delta t = 0.002$ s. The fluid is initially at rest, and no-slip boundary conditions are imposed. An example of the numerically simulated flow is given in Fig. 8, where the velocity field at $t = 150$ s for experiment B, but with $A_H = 10^{-4}$ m^2 s^{-1} (case DSGS, defined below), is shown.

In Fig. 5 the solid lines denote the velocity profiles at $y = 10$ cm (i.e., in the middle of the region Σ, Fig. 3), over which the averaging was performed giving the bars in the same graphs) obtained by solving Eq. (10) with A_H given by the molecular viscosity for water ($A_H = 10^{-6}$ m^2 s^{-1}). Let us first consider experiment B, taken as the reference example in the preceding subsection. The numerical solution for real water matches very closely the experimental result for $x \geq 5$ cm; no data are available closer to the boundary, but for $x < 5$ cm we

could not expect agreement as the spatial resolution of the model does not allow for the viscous boundary layer to be resolved, as with the laboratory data, since $\delta_M < \Delta x$.

A first consequence of such good agreement is that the effect of bottom friction, which is absent in the mathematical model, is therefore totally negligible as far as the shape of the meridional velocity profile is concerned, which we could expect in advance in view of the small value of B compared to that of ε (see section 3b). The same can be said of the parabolic shape of the free surface in the laboratory experiments owing to the rotation of the tank, which is obviously absent in the mathematical model. This good agreement also implies a successful validation of the mathematical model and gives confidence to other numerical results. We therefore proceed to simulate numerically a flow [denoted as the dynamically similar Gulf Stream (DSGS) case] that is fully dynamically similar to the GS case so that we will then be able to assess and interpret the effect of the departure from similarity between the RT and the GS.

A DSGS is achieved by choosing a fictitious viscosity $A_H = 10^{-4}$ m^2 s^{-1} in the mathematical model in which $\varepsilon = 0.28$, $E = 5.7 \times 10^{-3}$, Re = 49 (recall that, for GS, $\varepsilon = 0.25$, $E = 5 \times 10^{-3}$, Re = 50). The result is shown by the dashed line in Fig. 5 (see experiment B; its comparison with the solid line representing the RT case shows an identical profile of the meridional velocity east of the viscous boundary layers, in agreement with the hypothesis put forward in subsection 3b). Moreover, the DSGS profile shows a viscous boundary layer that appears to be of the Munk type, in both shape and width ($\delta_M \approx 10$ cm). A feature worth noticing is that the inertial part of the DSGS profile is shifted away from the boundary with respect to the RT profile by an offset $L_0 \approx 7$ cm.

The remaining three cases (experiments A, C, and D, already discussed in section 3a) also compare well with the numerical simulations but, as shown in Fig. 5, there are important differences with respect to experiment B.

In experiment A the profile obtained with the viscosity of real water (solid line) accurately reproduces the experimental data westward of the stagnation line (located at $x \sim 30$ cm), but the experimental counterflow (for $x > 30$ cm) is much weaker than the simulations. What is the reason of this discrepancy? The counterflow is partly due to a southward recirculation of the jet west of island A (see Fig. 8); now, while in the numerical simulation the width of the main channel is 190 cm (matching experiment B), allowing for a numerical counterflow to develop, in the laboratory experiment A the distance was only 120 cm (line d turns into line e), and with such a narrow channel the water recirculates almost entirely through the gap north of island A, thus remarkably reducing the counterflow.

The agreement between bars and solid lines in experiments C and D is also good, although the experimental flow is slightly weaker than the numerical one in C and the numerical solution is slightly larger than the experimental one in D for $x > 30$ cm. This is likely due to the fact that in these experiments the asymptotic steady state could not be fully reached, as discussed in section 3a; moreover, in experiment D the sensible discrepancy between experimental and numerical profiles away from the western boundary is also due to the effect of the eastern coast (given by the line e of Fig. 1 in this experiment), which is located too close to the western coast to allow for a sufficiently extended zonal profile to fully develop at this very high intensity flow. As far as the comparison between small (RT) and large (DSGS) viscosity cases is concerned, while for experiment A the relation between the solid and dashed lines is the same as the one discussed for experiment B, a different behavior is found for experiments C and D. From a comparison with experiments A and B, the offset L_0 that separates solid and dashed lines decreases in C and virtually vanishes in D. This behavior must be due to nonlinear inertial effects.

In summary, a mathematical model, successfully validated with our experimental data, has allowed us to simulate numerically what was impossible to simulate experimentally, that is, a flow (DSGS) that is almost exactly dynamically similar to the Gulf Stream (GS) case but differs from the rotating tank experiment B (RT) only by a viscosity that is chosen to be 100 times larger than the molecular viscosity of water. The zonal structure of the meridional velocity of such a flow is found to have, away from the viscous boundary layer (which appears to be of the Munk type), a nearly exponential profile typical of inertial WBCs (e.g., Fofonoff 1954), with width $\sim\delta_I$. Moreover, the comparison between DSGS and RT shows that they are virtually coincident outside the viscous boundary layer, apart from an offset that is $L_0 \approx 7$ cm for experiments A and B (Re $\sim$ 25–50) and $L_0 \approx 0$ for experiment D (Re $\sim$ 150). This is a relevant result for laboratory modeling of WBCs, because it suggests how to extend to real flows the results obtained from rotating tank experiments performed with water, for which the horizontal Reynolds numbers are necessarily larger than those of naturally turbulent WBCs.

Finally, it is worth noticing that the DSGS profile is in substantial agreement with the near-surface velocity structure of the Gulf Stream reported by Rossby and

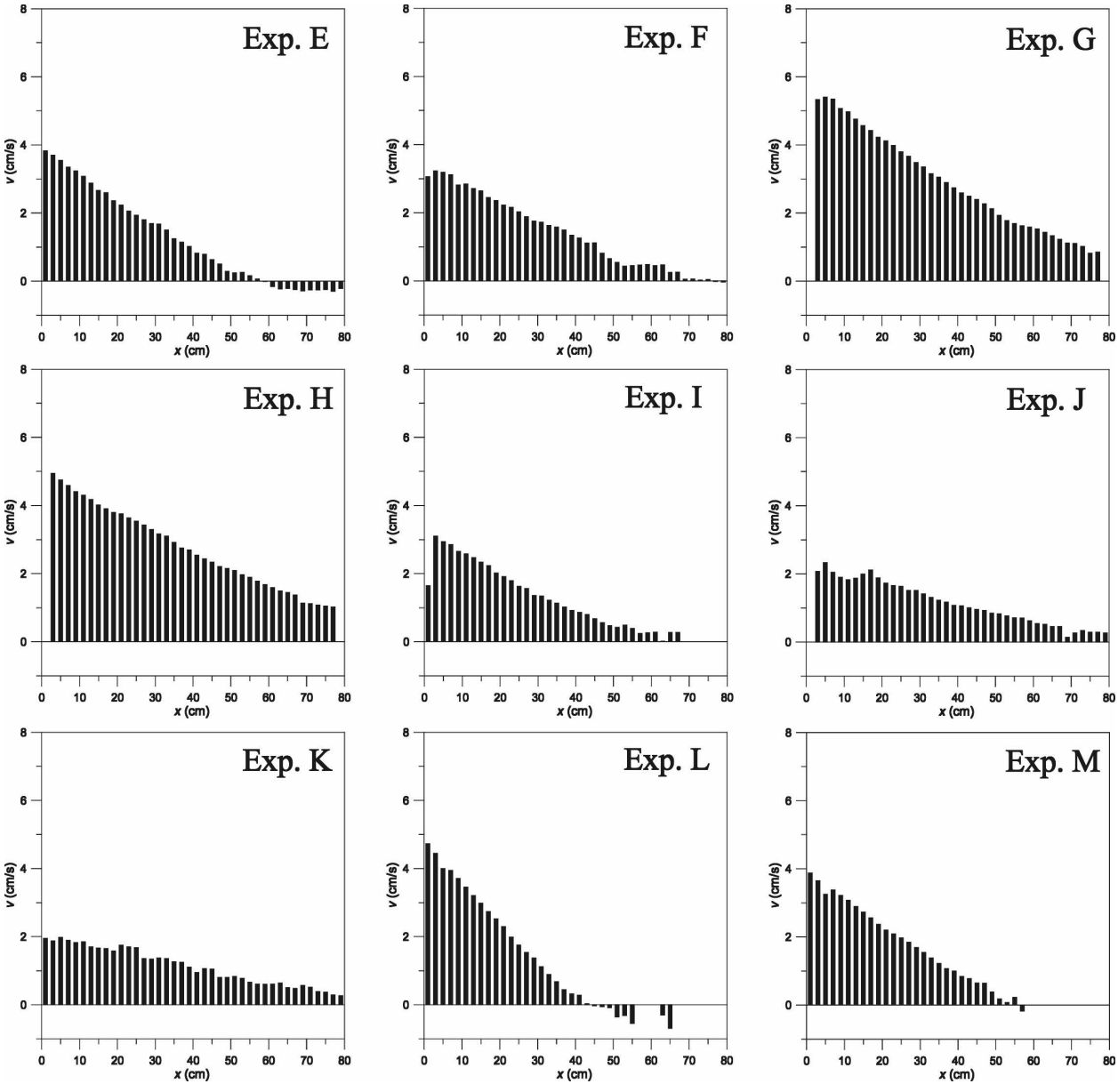

FIG. 9. Zonal profiles of the alongshore component v of the velocity obtained by photogrammetry for the expts E through V (see Table 1). Each bar represents a velocity centered at $y = 10$ cm averaged spatially over a sector 2 cm wide in the x direction and within the interval (0, 20 cm) in the y direction; the velocity is averaged over the intervals (80 s, 240 s) for expts E, F, I, J, K, L, M, N, R, S, T, U, and V, and (60 s, 130 s) for expts G, H, O, P, and Q.

Zhang (2001), obtained by ADCP and XBT measurements. The stream-averaged velocity profile shows a double-exponential pattern (their Fig. 2). The inner exponential (decreasing toward the coast) lies over shoaling water, so it has no counterpart in our experiments. The outer exponential (decreasing offshore) lies over deep water and is fairly well represented by the dashed line of Fig. 5 and experiment B therein, to the right of the maximum velocity, in shape, amplitude, and width (see the GS scaling in Table 2).

4. Other experiments

The remaining experiments, representing possible WBC states, can be divided into three groups (see Table 1 and Fig. 9). In a first group, from experiments E through K (including B and C, already discussed), a thin island A (Fig. 1) was used: in other words, the WBCs were produced in a wide channel of 1.9 m (which is the distance between lines c and d). The second group includes experiments L through T: these are the same

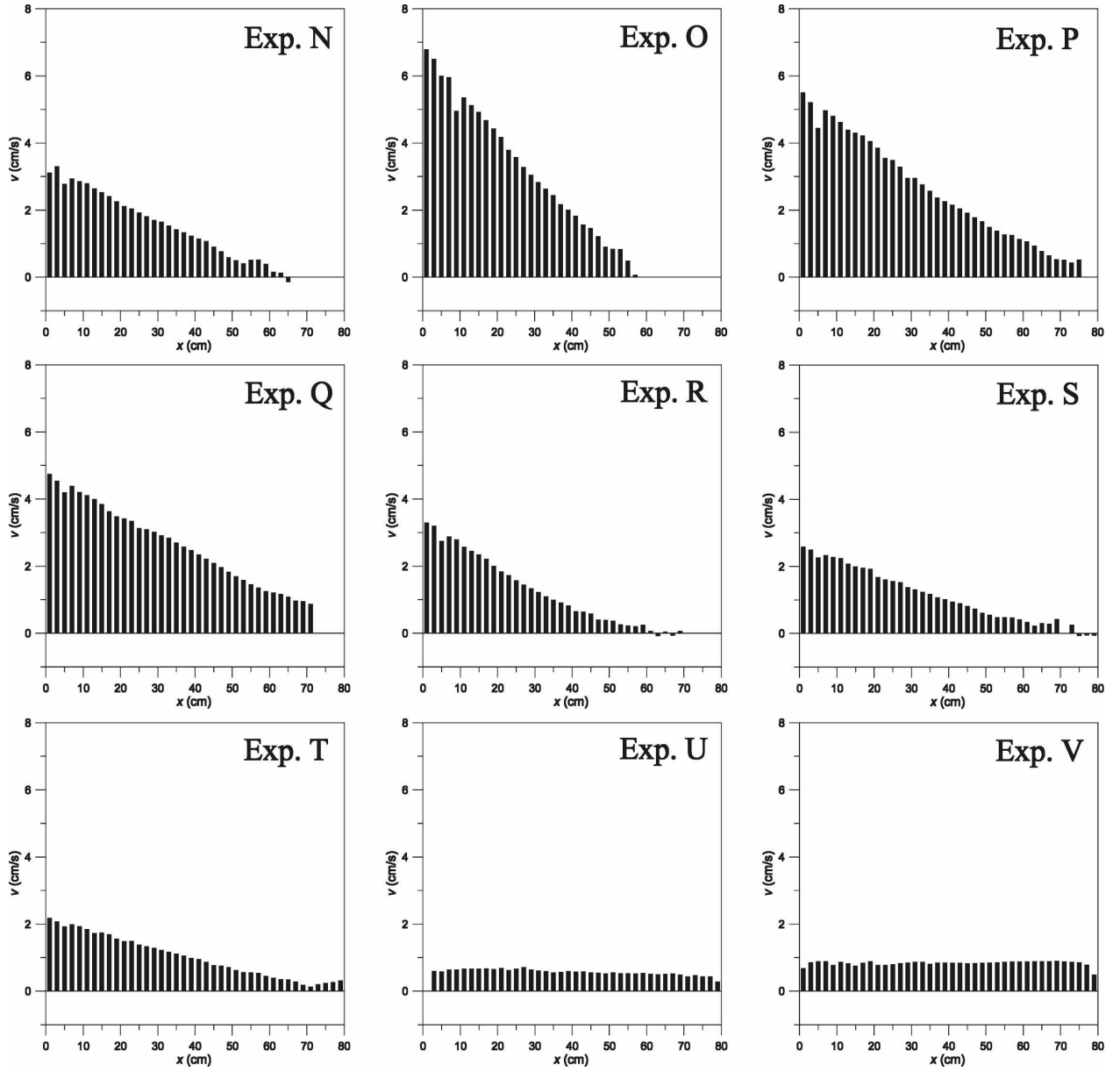

FIG. 9. (*Continued*).

experiments of the first group but performed with a wider island A corresponding to a width of the channel of only 1.2 m (which is the distance between lines c and e). Finally, the third group includes two trivial sensitivity experiments (U and V) aimed at verifying the lack of westward intensification in the absence of the beta effect or rotation.

The first group of experiments is divided into three sets, each of them including three experiments that differ only by the rotation rate of the tank T_{rot} (30, 45, and 60 s). From the dependency $\beta^* \propto {T_{\mathrm{rot}}}^{-1}$, an increase of T_{rot} produces an increase of both nonlinear ($\varepsilon \propto T_{\mathrm{rot}}$) and viscous effects ($E \propto T_{\mathrm{rot}}$), while leaving Re, and obviously the total transport Q, unchanged. This sensitivity analysis is therefore complementary to the one presented in the preceding section for experiments A–D, where the increase of u_p leads to an increase of ε, Re, and the total transport, while leaving E unchanged (however, it should be noticed that, while variations of u_p are directly related to variations of the intensity of a WBC, variations of the beta effect have a mainly theoretical relevance). Let us consider the first set of three experiments—B, E, and F—all forced by a piston moving at a speed $u_p = 1$ cm s^{-1}. One can easily notice from

Fig. 9 that also in this case the dependence of the zonal extension of the flow is substantially given by δ_I [Eq. (7)]; that is, the stagnation point follows the law $x_s \propto \delta_I \propto \sqrt{T_{\rm rot}}$. Here, however, unlike experiments A–D (section 3a) for which $v_{\max} \propto \sqrt{T_{\rm rot}}$, the total volume transport remains constant, $Q \propto x_s v_{\max} \propto u_p = \text{const}$, which implies $v_{\max} \propto T_{\rm rot}^{-1/2}$ (always under the assumption of a substantially triangular shape of the profile, as confirmed by Fig. 9)from which it follows that the slope of the profile is different for each experiment. This expected dependence can, again, be easily verified by analyzing Fig. 9.

The second set of three experiments—C, G, and H—differs from the previous one only by the piston speed, which is now doubled: $u_p = 2$ cm s^{-1}. The results are again in agreement with the scaling arguments discussed above, but for the evaluation of x_s one must rely, for G and H, on an extrapolation of the data outside the region S by means of an exponential fitting, as done for experiment D (see section 3a). Finally, the third set of experiments—I, J and K—differs from the first set (B, E and F) only by a reduced bottom slope. The shallow region to the right of line g in Fig. 1 was lowered from a depth of 17 cm to a depth of 27.5 cm so that the topographic beta effects β^* in experiments I, J, and K are reduced by a factor of 0.46 compared to those of experiments B, E, and F, respectively. Therefore, the stagnation point (the maximum velocity) is expected to be shifted farther eastward (to be reduced) by a factor of 1.47 (by a factor of 0.68) according to the usual scaling arguments. The experimental results are once more in substantial agreement with these theoretical arguments, as can easily be verified by comparing the bar profiles of experiments B, E, and F with those of experiments I, J, and K (for experiments J and K an extrapolation for $x_s > 80$ cm must be performed here too). Apart from the comparison with experiments B, E, and F, the validity of the scaling arguments can also be verified within the set I, J, and K, as for the previous two sets.

The second group of experiments was carried out in order to assess the role played by the eastern coast (line d or e of Fig. 1) on the WBC structure. While in the first group the main channel was 1.9 m wide, for experiments L through T its width was reduced to 1.2 m. Both widths are much smaller, in scale, than the cross-shore extension of real oceans (although they are definitely larger than the length scale of the modeled WBCs), so it is useful to check whether the presence of the eastern coast may introduce spurious effects on WBC structure. The substantial agreement found between the homologous experiments of the two groups ensures that the obtained results are robust and they are, therefore, virtually the same as those that would be obtained in an infinitely wide ocean. The most evident difference is a small reduction of x_s in the narrow-channel experiments, especially in the high amplitude case (cf. experiments C, G, H with, O, P, Q, respectively); however this is not related to the width of the channel but is rather due to a slightly higher value of β^* in experiments L through Q, for which the value of $h_1 - h_2$ (see Table 1) was changed, for technical reasons, from 23 to 25 cm.

Finally, the third group includes two experiments (U and V) that may be considered trivial because their only purpose is to check the obvious lack of any westward intensification if either the beta effect (U) or rotation (V) is absent. The confirmation of this property (Fig. 9) is nonetheless useful because it emphasizes that the geometrical setup adopted does not introduce any important asymmetry in the zonal direction. Noting that in the two experiments the total transport is the same, the higher values of the velocity in experiment V compared to those of experiment U is simply due to the smaller depth at $y = 10$ cm in the former, compared to the latter, because in experiment U the depth is h_1 everywhere.

5. Conclusions

The use of a large rotating basin and a novel setup has allowed us to simulate experimentally highly nonlinear WBCs with a wide zonal section. Among the many aspects of the experiments, the following may be emphasized: (i) the planetary beta effect necessary for the westward intensification was modeled through an equivalent topographic effect in a wide rectangular channel; (ii) the wind-driven Sverdrup return flow that feeds the WBC in a real oceanic subtropical or subpolar gyre was substituted by a flow produced remotely by a piston, moving along a rectangular channel parallel to the one where the WBC is generated; and (iii) the zonal profile of the meridional velocities of the almost steady WBCs thus generated was much wider [O(1 m)] than that usually obtained in smaller tanks with classical sliced cylinder or cone models, and was measured photogrammetrically over a region of about 1 m^2.

In all of the experiments performed Re $\gg 1$. The zonal profiles of the alongshore velocity are always found to have a nearly exponential profile away from the viscous boundary layer, with typical length scale $\sim\delta_I$. A control experiment (B) is analyzed in detail: it has the same ε as the Gulf Stream (GS) but much smaller E. This implies that the laboratory flow is expected to be geometrically similar to the GS outside the viscous boundary layer but not within it. To analyze such departure from dynamic similarity, a shallow-

water numerical model was used that allowed us to simulate a flow (called DSGS) fully dynamically similar to the GS. The comparison between the profile thus obtained numerically and the one obtained experimentally shows that they are indeed virtually coincident outside the viscous boundary layer, except for a small offset that tends to vanish as $\mathrm{Re}\to\infty$. This is a relevant result, as far as the laboratory modeling of WBCs is concerned, because it suggests how to extend, to real geophysical flows, results obtained from experiments performed in rotating tanks with water for which the horizontal Reynolds numbers are (at least in the present experimental setup) necessarily larger than those of naturally turbulent WBCs.

A set of experiments differing only by the piston speed has revealed the effect of nonlinearities. The zonal profile of the alongshore velocity is found to have a nearly triangular shape west of the position x_s of the stagnation line. Moreover, it is found that both the base x_s and the height $v_{\max}$ of such a triangle are dependent on the square root of the paddle speed u_p: as a consequence, the mean slope of the velocity profile is virtually independent of the total transport Q, which in turn is proportional to u_p ($Q \propto x_s v_{\max} \propto u_p$) in the strongly nonlinear parameter range considered. While the dependency $x_s \propto \sqrt{u_p}$ could be expected, as it is in agreement with the classical boundary layer scale δ_I of purely inertial WBCs, the same dependency for $v_{\max}$ (implying a virtually constant mean slope of the velocity profile) was found as well. In addition, sensitivity experiments in which the rotation rate of the basin, the topographic beta effect, and the width of the channel are varied have been carried out. They provide further information on the dependence of the zonal structure of WBCs on the various parameters in a strongly nonlinear regime.

Possible future developments concern the analysis of a series of effects, not included in the present experimental setup, that could be taken into account in an extended version of the system. The introduction of a sloping sidewall along the western boundary (line *c* in Fig. 1) would permit analysis of the effect of a shelf and slope bottom topography, as done in the sliced cone model in a very different setup. The possibility of reducing the width of the channel where the piston moves would allow one to simulate weakly nonlinear or even quasi-linear WBCs that, though less realistic than those analyzed here, could be compared with classical analytical results. The process of the separation of a WBC from the coast could be analyzed as well. In relation to this, in a recent numerical modeling study of the low-frequency variability of the Kuroshio Extension (Pierini 2006, 2008), the fundamental role played by the shape of the coast south of Japan in the separation of the Kuroshio was recognized. Such a process could, therefore, be studied in laboratory experiments based on a setup similar to the one used for the present research, provided the straight meridional coast is replaced by a coast with a schematic profile mimicking real topography. The instability mechanisms producing the subsequent relaxation oscillations and meandering of a separated jet could be analyzed as well.

Acknowledgments. The laboratory experiments presented in this paper were carried out at SINTEF (Trondheim, Norway) with the support of the European Commission through the "Programme for Improving the Human Research Potentials/Access to Major Research Infrastructures" (Contract HPRI-CT-1999-00060). We thank anonymous referees for valuable suggestions that improved our presentation.

REFERENCES

Baines, P. G., and R. L. Hughes, 1996: Western boundary current separation: Inferences from a laboratory experiment. *J. Phys. Oceanogr.,* **26,** 2576–2588.

Beardsley, R. C., 1969: A laboratory model of the wind-driven ocean circulation. *J. Fluid Mech.,* **38,** 255–271.

——, and K. Robbins, 1975: The "sliced-cylinder" laboratory model of the wind-driven ocean circulation. Part 1. Steady forcing and topographic Rossby wave instability. *J. Fluid Mech.,* **69,** 27–40.

Deese, H. E., L. J. Pratt, and K. R. Helfrich, 2002: A laboratory model of exchange and mixing between western boundary layers and subbasin recirculation gyres. *J. Phys. Oceanogr.,* **32,** 1870–1889.

Faller, A. J., 1981: The origin and development of laboratory models and analogues of the ocean circulation. *Evolution of Physical Oceanography: Scientific Surveys in Honor of Henry Stommel,* B. A. Warren and C. Wunsch, Eds., MIT Press, 462–479.

Fofonoff, N. P., 1954: Steady flow in a frictionless homogeneous ocean. *J. Mar. Res.,* **13,** 254–262.

Gill, A. E., 1982: *Atmosphere–Ocean Dynamics*. Academic Press, 662 pp.

Greenspan, H. P., 1969: A note on the laboratory simulation of planetary flows. *Stud. Appl. Math.,* **48,** 147–152.

Griffiths, R. W., and G. Veronis, 1997: A laboratory study of the effects of a sloping side boundary on wind-driven circulation in a homogeneous ocean model. *J. Mar. Res.,* **55,** 1103–1126.

——, and ——, 1998: Linear theory of the effect of a sloping boundary on circulation in a homogeneous laboratory model. *J. Mar. Res.,* **56,** 75–86.

——, and A. E. Kiss, 1999: Flow regimes in a wide "sliced-cylinder" model of homogeneous beta-plane circulation. *J. Fluid Mech.,* **399,** 205–236.

Helfrich, K. R., J. Pedlosky, and E. Carter, 1999: The shadowed island. *J. Phys. Oceanogr.,* **29,** 2559–2577.

Hendershott, M. C., 1987: Single layer models of the general circulation. *General Circulation of the Ocean,* H. D. I. Abarbanel and W. R. Young, Eds., Springer-Verlag, 202–267.

Kiss, A. E., 2001: Dynamics of laboratory models of the wind-

driven ocean circulation. Ph.D. thesis, Australian National University, 150 pp.

Løvås, S. M., 2003: HYDRIV Task 4: Modernization and improvement of 3D particle tracking using three synchronous cameras for near real-time analysis. SINTEF Rep. STF80 A038059, 10 pp.

——, T. A. McClimans, and E. Manent, 2001: The use of photogrammetry for measuring vertical velocities in laboratory geophysical dynamics experiments. *Proc. Third Int. Symp. on Environmental Hydraulics,* Tempe, AZ, International Association for Hydraulic Research (IAHR), 6 pp.

Munk, W. H., 1950: On the wind-driven ocean circulation. *J. Meteor.,* **7,** 80–93.

Nilsen, J. H., and I. Hådem, 1994: Photogrammetric tracking of tracer particles in modelled ocean flows. *J. Photogramm. Remote Sens.,* **49,** 9–20.

Pedlosky, J., 1965: A note on the western intensification of the oceanic circulation. *J. Mar. Res.,* **23,** 207–209.

——, 1987: *Geophysical Fluid Dynamics*. 2nd ed. Springer-Verlag, 710 pp.

——, 1996: *Ocean Circulation Theory*. Springer, 453 pp.

——, and H. P. Greenspan, 1967: A simple laboratory model for the oceanic circulation. *J. Fluid Mech.,* **27,** 291–304.

——, L. J. Pratt, M. A. Spall, and K. R. Helfrich, 1997: Circulation around islands and ridges. *J. Mar. Res.,* **55,** 1199–1251.

Pierini, S., 1996: Topographic Rossby modes in the Strait of Sicily. *J. Geophys. Res.,* **101,** 6429–6440.

——, 2006: A Kuroshio Extension system model study: Decadal chaotic self-sustained oscillations. *J. Phys. Oceanogr.,* **36,** 1605–1625.

——, A. M. Fincham, D. Renouard, M. R. D'Ambrosio, and H. Didelle, 2002: Laboratory modeling of topographic Rossby normal modes. *Dyn. Atmos. Oceans,* **35,** 205–225.

Pierini, S., 2008: On the crucial role of basin geometry in double-gyre models of the Kuroshio Extension. *J. Phys. Oceanogr.,* **38,** in press.

Rahmstorf, S., 1997: Risk of sea-change in the Atlantic. *Nature,* **388,** 825–826.

——, 1999: Shifting seas in the greenhouse? *Nature,* **399,** 523–524.

Rossby, T., and H.-M. Zhang, 2001: The near-surface velocity and potential vorticity structure of the Gulf Stream. *J. Mar. Res.,* **59,** 949–975.

Stommel, H., 1948: The westward intensification of wind-driven ocean currents. *Trans. Amer. Geophys. Union,* **29,** 202–206.

Sverdrup, H. U., 1947: Wind-driven currents in a baroclinic ocean, with application to the equatorial currents of the eastern Pacific. *Proc. Natl. Acad. Sci. USA,* **33,** 318–326.